A STUDY ON HEAVY/LIGHT ATOM DISCRIMINATION IN BRIGHT-FIELD ELECTRON MICROSCOPY USING THE COMPUTER

JOACHIM FRANK

From the Jet Propulsion Laboratory, California Institute of Technology, Pasadena, California 91103. Dr. Frank's present address is the Department of Applied Physics, College of Engineering, Cornell University, Ithaca, New York 14850.

ABSTRACT The Z dependence of the phase angle of the complex atomic scattering amplitude can be used to separate the image due to the heavy atoms from that due to the light atoms of the object structure. The linear theory of image formation applied to a focus series of bright-field images leads to Schiske's formula for the calculation of the structure factor. A program system is described which uses this algorithm for computing both images from a set of digitized electron micrographs of a focus series of uranyl-stained DNA on a thin carbon film.

INTRODUCTION

It is known that Born's first approximation is insufficient to describe the elastic scattering of electrons on atoms (Glauber and Schomaker, 1953). Better approximations yield complex atomic scattering amplitudes $|f(\vartheta)|\ e^{i\eta(\vartheta)}$. The imaginary portion of the scattering is often referred to as the *anomalous* scattering. The importance of the imaginary portion for the electron microscopic image has been emphasized by a number of authors (Zeitler and Olsen, 1967; Reimer, 1969; Hoppe, 1970).

The phase angle η has been shown to be strongly dependent on the atomic number Z (Ibers and Vainshtein, 1962; Ibers and Hoerni, 1962; Haase, 1968, 1970). This fact can be used in bright-field electron microscopy for discriminating between portions of the object which consist of either light or heavy atoms (Hoppe, 1970). Theoretically, the respective information about the object can be obtained from a set of at least two electron micrographs taken at different focus values (Hoppe, 1970; Schiske, 1968). Besides this, other methods have been proposed (Hoppe et al., 1970 *b*) which require changes to the ray path in the electron microscope and could not yet be implemented for experimental reasons.

The purpose of this work is to show that the use of a focus series for heavy/light atom discrimination yields reasonable results, although only the coherent elastic part of the scattered wave is considered in the theory underlying the calculation. Results of earlier studies on Ferredoxin by Bussler and Hoppe were mentioned in the lecture by Frank et al. (1970 *a*).

Heavy/light atom discrimination is a promising tool in the field of molecular biology, since it can be used for visualizing marker atoms which are attached to biological molecules at known sites. Because of the density fluctuations of the supporting film, the *direct* detection of single atoms in the image produced by the conventional electron microscope is not possible under bright-field illumination. There is some evidence that dark-field visualization of single heavy atoms can now be accomplished under favorable conditions (Whiting and Ottensmeyer, 1971; Koller, 1971). A detailed discussion of element differentiation (Cosslett, 1965) shows that, under the usual working conditions of the conventional electron microscope, the effect of the atomic number is relatively weak in the image.

It is known that an efficient element discrimination can also be accomplished by using the Z dependence of the ratio of the inelastic to elastic portion of scattering in the scanning transmission electron microscope (Crewe and Wall, 1970).

THEORY

The Bright-Field Image in the Linear Approximation

First, the image formation in the case of coherent bright-field illumination will be outlined as far as it is relevant to the derivation of the algorithm used later.

For expediency, the following symbols are introduced to describe the Fourier transformations in two dimensions:

$$f(\mathbf{k}) = \mathfrak{F}\{a(\mathbf{r})\} = \iint_{-\infty}^{\infty} a(\mathbf{r}) \exp[2\pi i\mathbf{kr}]\, d\mathbf{r}, \tag{1}$$

$$a(\mathbf{r}) = \mathfrak{F}^{-1}\{f(\mathbf{k})\} = \iint_{-\infty}^{\infty} f(\mathbf{k}) \exp[-2\pi i\mathbf{kr}]\, d\mathbf{k}, \tag{2}$$

where $\mathbf{r} = (x, y)$ is the position vector in space and $\mathbf{k} = (k_x, k_y)$, the vector in Fourier space.

Under axial illumination, the elastic coherent portion of the scattered wave in the image plane can be described (Hoppe, 1970; Reimer, 1969; Uyeda, 1955) by the Kirchoff integral in the Fraunhofer approximation

$$\psi_s(\mathbf{r}) = \frac{A_0}{\lambda} i\,\mathfrak{F}^{-1}\{F(\mathbf{k})P(\mathbf{k})\}, \tag{3}$$

where A_0 is the amplitude of the plane monochromatic primary wave ψ_0. $F(\mathbf{k})$ is the structure factor of a plane arrangement of atoms in $r_j = (x_j, y_j)$, which is derived from the three-dimensional arrangement by projecting along the z axis:

$$F(\mathbf{k}) = \sum_j f_j(\mathbf{k}) \exp[-2\pi i \mathbf{k}\mathbf{r}_j], f_j \text{ atomic scattering amplitudes.} \qquad (4)$$

λ is the electron wavelength, and $P(\mathbf{k})$ the pupil function, which is composed of the aperture function $b(\mathbf{k})$ and the phase term $\exp[-i\gamma]$.

$$P(\mathbf{k}) = b(\mathbf{k}) \cdot \exp[-i\gamma(\mathbf{k})], \qquad (5)$$

$$b(\mathbf{k}) = \begin{cases} 1 \text{ within the aperture,} \\ 0 \text{ elsewhere;} \end{cases} \qquad (6)$$

$$\gamma(\mathbf{k}) \equiv \gamma(\vartheta, \phi) = \frac{\pi}{2\lambda} C_s \vartheta^4 - \frac{\pi}{\lambda}\left(\Delta z + \frac{\Delta z_A}{2} \sin 2[\phi - \phi_0]\right)\vartheta^2, \qquad (7)$$

with the following definitions:

$$\left.\begin{aligned} \vartheta \approx \sin\vartheta &= \lambda\sqrt{k_x^2 + k_y^2} \\ \phi &= \arctan(k_y/k_x) \end{aligned}\right\} \text{ polar coordinates in the aperture and in the Fourier plane, respectively.}$$

C_s = Spherical aberration of the objective lens.

Δz = Defocus value.

Δz_A = Focus difference of the axial astigmatism.

ϕ_0 = Reference angle of the axial astigmatism.

The term $\gamma(\mathbf{k})$ in equations 5 and 7 represents the phase shift produced by the lens aberrations and by the defocusing of the objective lens (Scherzer, 1949). This representation holds only for thin objects, i.e., objects with little extension in the direction of the incident primary beam. Additionally a phase shift of $\pi/2$ has been assumed in equation 3 as resulting from the elastic scattering (Eisenhandler and Siegel, 1966; Zeitler and Olsen, 1967).

The inelastic scattering will be neglected in our treatment although it is particularly strong for carbon (Lenz, 1954; Reimer and Sommer, 1968 *b*). It is assumed, however, that the image produced by inelastically scattered electrons is blurred by the effect of chromatic aberration (Crick and Misell, 1971) and that the phase contrast produced by the elastically scattered waves is the predominant source for the high resolution image contrast.

The coherent part of the scattered wave (equation 3) interferes with the primary wave and gives the complex amplitude in the image plane

$$\psi = \psi_0 + \psi_s, \qquad (8)$$

and the intensity

$$I = \psi\psi^* = A_0^2 + 2A_0 \operatorname{Re}\{\psi_s\} + \psi_s\psi_s^* = I_0 + I_B + I_D. \qquad (9)$$

If we restrict ourselves to the case of weakly scattering objects

$$|\psi_s| \ll |\psi_0|, \tag{10}$$

we can neglect the dark-field portion I_D of the image in equation 9. The Fourier transformation of the bright-field portion I_B gives

$$j(\mathbf{k}) = \mathfrak{F}\{I(\mathbf{r})\} = i[F(\mathbf{k})P(\mathbf{k}) - F^*(-\mathbf{k})P^*(-\mathbf{k})], \tag{11}$$

where equation 3 has been used and the unessential factor A_0^2/λ has been set to unity.

Definition 4 shows that the structure factor satisfies Friedel's law,

$$F(\mathbf{k}) = F^*(-\mathbf{k}), \tag{12}$$

as long as the atomic scattering amplitudes are real.[1] In this case, further assuming a symmetrical aperture function $b(\mathbf{k})$, equation 11 yields the well-known Fourier relation for "phase objects" (Thon, 1965; Hanssen, 1965):

$$j(\mathbf{k}) = 2b(\mathbf{k})F(\mathbf{k}) \sin \gamma(\mathbf{k}) \tag{13}$$

If, however, the imaginary part of the atomic scattering amplitude cannot be neglected,

$$f_j = f_j' + if_j'', \tag{14}$$

we obtain a representation comparable to equation 14 by putting

$$F(\mathbf{k}) = F_r(\mathbf{k}) + iF_i(\mathbf{k}), \tag{15}$$

where

$$F_r(\mathbf{k}) = \sum_j f_j' \exp[-2\pi i \mathbf{r}_j \mathbf{k}], \tag{16 a}$$

and

$$F_i(\mathbf{k}) = \sum_j f_j'' \exp[-2\pi i \mathbf{r}_j \mathbf{k}]. \tag{16 b}$$

Note that equation 15 shows a decomposition of $F(\mathbf{k})$ into one part which satisfies Friedel's law and one which does not.

Now equation 11 yields, by virtue of equation 5,

$$j(\mathbf{k}) = 2b(\mathbf{k})\{F_r(\mathbf{k}) \sin \gamma(\mathbf{k}) - F_i(\mathbf{k}) \cos \gamma(\mathbf{k})\}, \tag{17}$$

---

[1] This is true only as long as the curvature of the Ewald sphere is neglected. If the structure factor is taken along the surface of the Ewald sphere rather than on the tangential plane, Friedel's law is not satisfied even with the $f(\mathbf{k})$ being real (Hoppe, 1970).

if $b(\mathbf{k})$ is again assumed to be symmetrical. Part F_r of the structure factor is still transferred as it is in the case of a pure phase object in equation 13, but now another term F_i is added, which is transferred with maximum contrast just at the zeros of the phase-contrast transfer function $\sin\gamma$ (Hanssen, 1965). This term is usually attributed to the amplitude scattering of the object and is responsible for the loss of electrons; however, as Reimer has pointed out (Reimer, 1969), the distinction between phase and amplitude contrast becomes difficult to make if complex atomic scattering factors are used. According to the optical theorem of the scattering theory (see, for instance, Messiah, 1962), the contrast due to the loss of elastically scattered electrons screened by the objective aperture is contained in expression 17 as far as the linear approximation of equation 9 is applicable.

A relationship similar to equation 17 has been used successfully by Erickson and Klug to describe their experimental results on electron micrographs of catalase crystals (Erickson and Klug, 1970).

It can be shown (to be published elsewhere), that the curvature of Ewald's sphere has mainly the effect of contributing an additional imaginary term $if'_j \sin(\pi\lambda\delta z_j\vartheta^2)$ in equation 14, with δz_j as the local focus deviation of the jth atom from the mean value Δz. This term becomes significant for high ϑ. For instance, if we take a carbon foil of 50 A, the contribution of top and bottom layer is $\pm if'_c \times 0.06$ at $\vartheta = 5 \times 10^{-3}$ rads, which exceeds if''_c considerably.

Properties of the Complex Image

We assume for a moment that $F(\mathbf{k})$ is already known within the aperture. Then the inverse transformation,

$$C(\mathbf{r}) = \mathcal{F}^{-1}\{b(\mathbf{k})F(\mathbf{k})\}, \tag{18}$$

yields a complex image, since $F(\mathbf{k}) \neq F^*(-\mathbf{k})$ as stated above. $b(\mathbf{k})$ is the aperture function introduced in equation 6. If $b(\mathbf{k})$ is a symmetrical function, we can separate the real and imaginary parts of the image in the form

$$\mathrm{Re}\,\{C(\mathbf{r})\} = \mathcal{F}^{-1}\{b(\mathbf{k})F_r(\mathbf{k})\} \tag{18 a}$$

$$\mathrm{Im}\,\{C(\mathbf{r})\} = \mathcal{F}^{-1}\{b(\mathbf{k})F_i(\mathbf{k})\} \tag{18 b}$$

We can write this result in a formal notation as a convolution of a set of delta functions representing the locations of the atoms in equation 4 with the "atomic images," i.e. the inverse transforms of the real and imaginary parts, respectively, of the atomic scattering amplitudes f_j. (For clarity, the aperture function, which would produce an additional convolution term in equations 19 *a* and 19 *b*, has been omitted.)

$$\mathrm{Re}\,\{C(\mathbf{r})\} = \sum_j \delta(\mathbf{r} - \mathbf{r}_j) \circ \mathcal{F}^{-1}\{f'_j(\mathbf{k})\}, \tag{19 a}$$

$$\mathrm{Im}\,\{C(\mathbf{r})\} = \sum_j \delta(\mathbf{r} - \mathbf{r}_j) \circ \mathfrak{F}^{-1}\{f_j''(\mathbf{k})\}, \tag{19 b}$$

where

$$f(\mathbf{r}) \circ g(\mathbf{r}) = \iint f(\mathbf{r}' - \mathbf{r})g(\mathbf{r}')\, d\mathbf{r}'.$$

This notation means that two images of the same two-dimensional point structure are produced. In each point of this structure, an atomic image function can be visualized which is either due to the real or to the imaginary scattering.

Since the resolution in the original electron micrographs is limited by the lens aberrations, we can expect that the resolution in the calculated images, equations 18 *a* and 18 *b*, is improved considerably. If we assume that $F(\mathbf{k})$ can be determined without error, then the resolution in equations 18 *a* and 18 *b* is limited only by the aperture and the mechanical and electrical stability of the electron microscope.

Calculation of the Structure Factor Using a Focus Series

Equation 11 yields a set of equations

$$j_n(\mathbf{k}) = \begin{cases} i(F(\mathbf{k}) \exp[-i\gamma_n] - F^*(-\mathbf{k}) \exp[+i\gamma_n]) & \text{within the aperture,} \\ 0 & \text{elsewhere,} \end{cases} \tag{20}$$

between the Fourier coefficients of the image and the values of the structure factor for each different phase function $\exp[-i\gamma]$. Provided that the phase factors are known from an independent measurement, it is sufficient for the calculation of $F(\mathbf{k})$ and $F^*(-\mathbf{k})$ to have two electron micrographs of the same object with different defocus Δz.

It is assumed that the structure of the object remains unchanged during the two subsequent exposures. It should be emphasized that this assumption is very restrictive, since some studies on radiation damage (Glaeser et al., 1970) indicate that the structural details corresponding to higher resolution are distorted within a short time, at least under the usual illumination (Williams and Fisher, 1970) and vacuum conditions (Hartmann and Hartmann, 1971).

By solving equation 20 for two micrographs ($n = 1, 2$), we obtain

$$F(\mathbf{k}) = \frac{j_1 \exp[i\gamma_2] - j_2 \exp[i\gamma_1]}{2 \sin(\gamma_2 - \gamma_1)}$$

$$\text{for } \gamma_1 \neq \gamma_2 + m\pi,\ m = 0, \pm 1, \pm 2 \cdots \tag{21}$$

The result has a formal singularity when $\gamma_1 = \gamma_2 + m\pi$. This type of singularity does also occur, if three or more micrographs are used (see next paragraph), but it can then easily be removed. Nevertheless it is valuable to use only two micrographs, if possible, because of radiation damage considerations mentioned previously. It is easily calculated that for $\lambda = 0.037$ A

$$0 < |\gamma_1 - \gamma_2| < \pi,$$

i.e. no singularity occurs, if $\vartheta < 10^{-2}$ rads and $|\Delta z_1 - \Delta z_2| < 370$ A, which is readily achieved on modern microscopes.

If, on the other hand, the object is sufficiently stable, or if only low resolution information is required, the accuracy of the calculation of $F(\mathbf{k})$ can be improved by using more than two images of the focus series. The resulting formula has already been established by Schiske (Schiske, 1968).[2] It is obtained if the overdetermined system, equation 20, with $n = 1, 2 \cdots N > 2$, is solved using the least squares method. The "normal equations" associated with the system are (Hildebrand, 1956 *a*):

$$\begin{aligned} F(\mathbf{k}) \sum_{m=1}^{N} \exp[-2i\gamma_m] - F^*(-\mathbf{k}) \sum_{m=1}^{N} \exp[i\gamma_m - i\gamma_m] \\ = -i \sum_{m=1}^{N} j_m(\mathbf{k}) \exp[-i\gamma_m], \\ F(\mathbf{k}) \sum_{m=1}^{N} \exp[i\gamma_m - i\gamma_m] - F^*(-\mathbf{k}) \sum_{m=1}^{N} \exp[2i\gamma_m] \\ = -i \sum_{m=1}^{N} j_m(\mathbf{k}) \exp[i\gamma_m], \end{aligned} \quad (22)$$

and immediately yield Schiske's formula

$$F(\mathbf{k}) = \frac{-i \sum_{m=1}^{N} j_m(\mathbf{k}) \exp[i\gamma_m] \left\{ N - \sum_{n=1}^{N} \exp[2i(\gamma_n - \gamma_m)] \right\}}{N^2 - \left| \sum_{m=1}^{N} \exp[-2i\gamma_m] \right|^2}. \quad (23)$$

It can be shown that equation 23 is equivalent to equation 21 for $N = 2$.

Problems with the Evaluation of Schiske's Formula

Determination of the Phase Factors. The phase factors $\exp[i\gamma]$ must be known for the evaluation of equation 23. A special method for determining the parameters Δz, Δz_A, ϕ_0 in $\gamma(\mathbf{k})$ (see equation 7) has already been reported (Frank et al., 1970 *a*, *b*). In this article, only the general idea will be outlined.

In many specimen preparations, a thin carbon film is used as an object support. Studying bright-field images of these carbon films, Thon has shown (Thon, 1965)

---

[2] Schiske starts with the "complex amplitude transparency" and its Fourier coefficients $c(\mathbf{k})$. Because of the phase shift $\pi/2$ produced by the elastic scattering, the latter are related to the structure factor by $c(\mathbf{k}) = iF(\mathbf{k})$.

that the intensity distribution in the optical diffractograms is, save for a radial dependence, described by the function $\sin^2 \gamma$, according to the transfer equation 13 for "pure phase objects."

If the image under consideration contains a portion due to an amorphous carbon film, a least squares procedure can be used which fits the amplitudes of the Fourier coefficients with the function $g(\vartheta) \mid \sin \gamma \mid$ by varying the parameters Δz, Δz_A, ϕ_0 in equation 7, starting from a set of initial values $\Delta z_i, \Delta z_{Ai}, \phi_{0i}$. The function $g(\vartheta)$ is used to match the radial dependence (Frank et al., 1970 *b*).

This procedure has to be repeated for each image used for the computation in equation 23. Fortunately, the focus *differences* can be reproduced in the electron microscope, and therefore the Δz values of the entire series are known within certain limits once the absolute value[3] Δz of *one* image has been determined. With the method described, the values of Δz can be determined within $\delta \Delta z = \pm 60$ A.

Phase Error of the Calculated Structure Factor. It follows from equation 7 that the phase error caused by an error of the defocus value $\delta \Delta z$ is

$$\Delta\gamma = \delta\Delta z \frac{\pi}{\lambda} \vartheta^2 . \qquad (24)$$

Hence, the maximum phase error within $\vartheta \leq 0.9 \times 10^{-2}$ for $\lambda = 0.037$ A and $\delta\Delta z = 60$ A is

$$\Delta\gamma_{\max} = 60 \times \frac{\pi}{0.037} \times 0.8 \times 10^{-4} \approx \frac{\pi}{8} . \qquad (25)$$

Now we shall consider the way in which the calculated structure factor, equation 23, is affected by an absolute phase error $\Delta\gamma$. We can write equation 23 in the form

$$F(\mathbf{k}) = -i \exp{[i\gamma_1]} \frac{\sum_{m=1}^{N} j_m(\mathbf{k}) \exp{[i(\gamma_m - \gamma_1)]} \left\{ N - \sum_{n=1}^{N} \exp{[2i(\gamma_m - \gamma_n)]} \right\}}{N^2 - \left| \sum_{m=1}^{N} \exp{[-2i\gamma_m]} \right|^2}, \qquad (23')$$

where only the factor $\exp{[i\gamma_1]}$ is dependent on the *absolute* value of Δz. Suppose that the phase γ_1 and the other phases γ_m, $2 \leq m \leq N$, have the common error $\Delta\gamma$. Then it follows from equation 23′ that, instead of $F(\mathbf{k})$, the Fourier coefficient $F'(\mathbf{k}) = F(\mathbf{k}) \exp{[i\Delta\gamma]}$ is calculated.

Since we have

$$F(\mathbf{k}) = F_r(\mathbf{k}) + iF_i(\mathbf{k})$$

---

[3] Since the errors of the parameters C_s, Δz, and M (= magnification) can balance each other within certain limits, and, on the other hand, both C_s and M can be determined only within 5%, the term "absolute value of Δz" simply means the value of Δz which is calculated by the least squares procedure for a given estimate of the parameters (M, C_s) within their respective error margins.

(equation 15), we obtain

$$F'(\mathbf{k}) = F_r(\mathbf{k}) \exp[i\Delta\gamma] + iF_i(\mathbf{k}) \exp[i\Delta\gamma], \tag{26}$$

and

$$F_r'(\mathbf{k}) = \tfrac{1}{2}[F'(\mathbf{k})] + F'^*(\mathbf{k})] = F_r(\mathbf{k}) \cos \Delta\gamma - F_i(\mathbf{k}) \sin \Delta\gamma, \tag{27 a}$$

$$F_i'(\mathbf{k}) = \frac{1}{2i}[F'(\mathbf{k}) - F'^*(\mathbf{k})] = F_r(\mathbf{k}) \sin \Delta\gamma + F_i(\mathbf{k}) \cos \Delta\gamma. \tag{27 b}$$

This means that the portions F_r and iF_i of the structure factor are redistributed in another way, dependent on ϑ. On a circle in the Fourier plane, where $\Delta\gamma = \pi/2$, F_r and F_i have exchanged places.

It becomes clear from equations 24, 27 *a*, and 27 *b* that the higher order coefficients are most sensitive to a wrong measurement of the absolute focus value. Taking $\Delta\gamma_{\max} = \pi/8$ from equation 25, equations 27 *a* and 27 *b* yield, at the aperture limit,

$$F_r'(\mathbf{k}) = 0.925\, F_r(\mathbf{k}) - 0.38\, F_i(\mathbf{k}),$$

$$F_i'(\mathbf{k}) = 0.38\, F_r(\mathbf{k}) + 0.925\, F_i(\mathbf{k}).$$

Singularities of Schiske's Formula. The neighborhood of $\vartheta = 0$ requires special consideration because the phases γ_m and the denominator in equation 23 go to zero. For $\gamma \ll 1$, we can approximate all exponential functions by $\exp[i\gamma] \approx 1 + i\gamma$. Now equation 23 yields

$$F(\mathbf{k}) \approx -\frac{\sum_{m=1}^{N} j_m(\mathbf{k})(1 + \gamma_m) \sum_{n=1}^{N} (\gamma_n - \gamma_m)}{2\left(\sum_{m=1}^{N} \gamma_m\right)^2}.$$

Obviously, part $F_r(\mathbf{k}) = 1/2[F(\mathbf{k}) + F^*(-\mathbf{k})]$ goes to infinity as $1/\gamma \sim 1/\vartheta^2$ when ϑ approaches zero, whereas the most interesting part, $F_i(\mathbf{k}) = 1/2i[F(\mathbf{k}) - F^*(-\mathbf{k})]$, remains finite.

Another singularity occurs when

$$\vartheta^2 = \frac{\lambda}{|\Delta z_s|}, \tag{28}$$

with Δz_s denoting the focus step $\Delta z_{m+1} - \Delta z_m$. In this zone, the phase difference between the phase shifts (equation 7) of subsequent images of the series becomes π, and therefore both the denominator and the factor in the numerator of equation 23 go to zero again. With $\lambda = 0.037$ A, we obtain from equation 28 the condition $\Delta z_s = 370$ A, if the aperture $\vartheta_a = 1 \times 10^{-2}$ rads is chosen. In the vicinity of this singularity, equation 23 must be replaced by

$$F(\mathbf{k}) = -i \sum_{m=1}^{N} j_m(\mathbf{k}) \exp [i\gamma_m].$$

Checking the Result. After the structure factor has been determined using equation 23, the consistency of the result with theory may be examined by calculating the Fourier coefficients j'_n (k) of the defocused images in the linear approximation of equation 9, using equation 20. The inverse transformation of the coefficients j'_n (k) should yield a series of images which are quite similar to the respective original images of the focus series. There are, however, a number of reasons why they cannot be expected to be identical:

(*a*) The object may have changed during the exposure of the focus series.
(*b*) The theory is confined to monochromatic coherent illumination.
(*c*) The inelastic scattering has been neglected.
(*d*) The dark-field term I_D in equation 9 has been neglected.

It should be mentioned that this test does not answer the question of whether the right set of defocus values has been applied in the calculation of the phase factors in equation 23 since, for any set of phase factors, this formula gives solutions which fulfill equation 20 in an optimal way.

Estimation of the Contrast

It is difficult to make predictions about the contrast in the real and imaginary images (equations 18 *a* and 18 *b*), since only few data are available on the atomic scattering amplitudes of atoms bound in the solid state (Reimer and Sommer, 1968 *a*). It is known (Lenz, 1954; Uyeda, 1955) that the behavior of the atomic scattering factors for small angles is determined by the type of binding, i.e., by the shape of the potential function far distant from the center of the atom. Therefore, the calculations of the atomic scattering amplitudes for single atoms, and any contrast estimation based upon them as well, will give only a rough idea of the actual contrast due to *bound* atoms.

In order to compare the intensities in the *center* of the atomic image in the real and imaginary parts of $C(\mathbf{r})$ and in the original image, respectively, we have to calculate the integrals

$$\mathrm{Re}\{C(\mathbf{r})\} = \frac{4\pi}{\lambda} \int_0^{\vartheta_a} f'(\vartheta) \sin \vartheta \, d\vartheta, \qquad (29\ a)$$

$$\mathrm{Im}\{C(\mathbf{r})\} = \frac{4\pi}{\lambda} \int_0^{\vartheta_a} f''(\vartheta) \sin \vartheta \, d\vartheta, \qquad 29\ b)$$

$$I_B = \frac{4\pi}{\lambda} \int_0^{\vartheta_a} \{f'(\vartheta) \sin \gamma_n(\vartheta) - f''(\vartheta) \cos \gamma_n(\vartheta)\} \sin \vartheta \, d\vartheta. \qquad (29\ c)$$

These integrals derive from the defining integral of the Fourier transform (see equation 2) with $\mathbf{r} = (0, 0)$. The last expression, equation 29 *c*, follows from equations 8 and 17 for a "structure" consisting of one atom only.

The integrals 29 *a*–29 *c* were calculated for uranium and carbon with reference to the particular object to be studied later. The values calculated by Haase from Thomas-Fermi-Dirac potentials for free atoms (Haase, 1970) were used for $f(\vartheta)$ (see Fig. 1). The ratios of these integrals calculated for uranium to those calculated for carbon may be considered a rough measure for the separation of the different atomic species in the respective images. We find 4:1, 50:1, and 3:1 in equations 29 *a*, *b*, and *c*, respectively, for $U = 100$ kv, $\vartheta_a = 0.9 \times 10^{-2}$ rads, and $\Delta z = 0$ A.

Although the results obtained for free atoms are not applicable to bound atoms in a quantitative sense, they can still be used as an estimate for the order of magnitude of the separation effect. We can therefore expect the image of a single uranium atom to appear fairly well separated from the carbon background in the *imaginary* part of the image, even if the thickness of the carbon film corresponds to 50 layers of atoms.

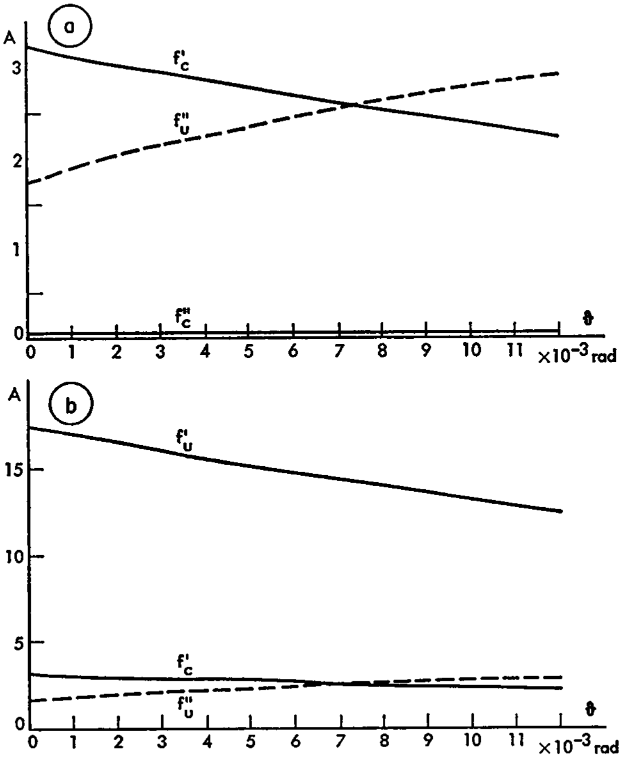

FIGURE 1 Complex atomic scattering amplitudes for free carbon and uranium atoms (after Haase, 1970). An enlarged scale is used in Fig. 1 *b* to show f_c''.

MATERIALS AND METHODS

The Focus Series

A focus series of a stained DNA molecule on carbon film was chosen for the application of the element discrimination technique because the possibility of electron microscopic base sequence analysis has been under discussion for some time (Beer and Moudrianakis, 1962; Moudrianakis and Beer, 1965; Zobel and Beer, 1961). All attempts to visualize the configuration of DNA molecules with the aid of heavy atom markers have failed, although some periodicities in the image could be related to the internucleotide distance (Fiskin and Beer, 1968). Recently, structural features in dark-field images of a DNA preparation have been reported (Ottensmeyer, 1969).

The focus series was provided by Dr. Walther Stoeckenius, San Francisco Medical Center, University of California, San Francisco, Calif. A thymus preparation (Worthington Biochemical Corp., Freehold, N. J.) of double-stranded DNA was deposited from solution onto a thin ($\sim$40 A) carbon film and stained for 30 min at 60°C in a 7.5% solution of uranyl magnesium acetate, and then briefly rinsed in 50% ethanol. The preparation was examined in a Siemens Elmiskop 101 (Siemens AG, Berlin, W. Germany) at ×395,000 magnification (intermediate lens pole piece used) using a cooled specimen chamber at liquid nitrogen temperature. Further specifications are:

Voltage	100 kv
Condenser aperture	200 μ
Objective lens	
Focal length	2.7 mm
Spherical aberration	2.9 mm
Aperture	60 μ
Recording	
Material	Kodak lantern slide plates (Eastman Kodak Co., Rochester, N. Y.)
Development	4 min at 20°C in D-19 (Kodak)

Quantitative studies on the interaction of DNA with uranyl salts suggest that the UO_2^{++} ions are preferably attached to the phosphate groups and that, at a concentration as high as that used for our preparation, some nonspecific attachment occurs as well (Zobel and Beer, 1961). Therefore, we cannot assume that only single uranyl ions are present, nor that only the nucleotides of the molecule are labeled. Clearly, for carefully testing the new method, a specimen should be chosen which is chemically well defined. The author hopes that this will be possible in future experiments.

The "macroscopic" photographic density range on the photo plates was measured using a 1-mm-diameter aperture (25 A on the object scale). The densities were 0.88 at the carbon film and 0.80 at the site of the DNA molecule (for comparison, see Figs. 8 *a–d*).

Video Input/Output and Computer Facilities

The electron micrographs of the series under investigation were copied from the photo plates onto fine-grain film material (Kodak Aerial Film SO-243). The transfer function of this film decreases less than 2% within the spatial frequency range of 0–10 cycles/mm, which carries the information about the object on electron micrographs at × 395,000 magnification. Therefore the resolution is not impaired by the copying procedure. Since the contribution of the photographic noise of the *original* micrographs is also very small in this spatial frequency range, no effort was made to examine the propagation of noise in equation 23.

An area of 30 × 30 mm, corresponding to 760 × 760 A at the × 395,000 magnification, was scanned with a video film converter (VFC) (Billingsley and Volkoff, 1969). The VFC is a cathode ray tube (CRT) film scanner–film recorder device. The spot diameter on the film and the scanning distance in both sample and line direction were 50 μ, corresponding to 1.27 A on the object scale. It is known (see, for instance, De Rosier and Moore, 1970) that the resolution is not affected as long as the scanning distance and the diameter of the scanning aperture are smaller than the resolution distance. The data were converted to digital form and written onto a magnetic tape in a six-bit representation.

Data processing on the IBM 360/44 computer and scanning were done at the Jet Propulsion Laboratory (JPL) Image Processing Laboratory. The programs were written in FORTRAN, using special I/O routines applicable to the Video Image Communication and Retrieval (VICAR) system. VICAR was designed at JPL to facilitate the acquisition, digital processing, and recording of image data (National Aeronautics and Space Administration, 1968). Programs for standard operations such as Fourier transformation, cross-correlation, and contrast stretching were available from a general applications program library (Billingsley, 1970). A detailed description of the JPL image processing system has recently been given by Billingsley (Billingsley, 1971).

The calculated images were displayed with a resolution of 50 × 50 μ using the VFC. The photographic density on the output picture was defined by the linear equation

$$\mathrm{d}(\mathbf{r}) = 2\frac{I(\mathbf{r}) - I_{\min}}{I_{\max} - I_{\min}}, \qquad (31)$$

where $I(\mathbf{r})$ are the image data.

The values for $I_{\min}$, $I_{\max}$ were taken at the "tails" of the histogram rather than the absolute extrema of I (see Fig. 2). The tails were defined as

$$H(I > I_{\max}) = 1\%,$$
$$H(I < I_{\min}) = 1\%, \qquad (32)$$

where H denotes the cumulative frequency with which the data are encountered in the specified range, normalized to the total number of picture elements. Outside the selected range of the histogram, the photographic density of the output picture was set to

$$d = d_{\max} = 2 \qquad I > I_{\max},$$
$$d = 0 \qquad I < I_{\min}. \qquad (33)$$

In all representations of Fourier transforms $G(\mathbf{k})$, only the values of $|G(\mathbf{k})|$ were of special interest. Since these values vary in a range of two orders of magnitude, a logarithmic representation was chosen, so that the photographic density on the output picture is proportional to

$$\log |G(\mathbf{k})|. \qquad (34)$$

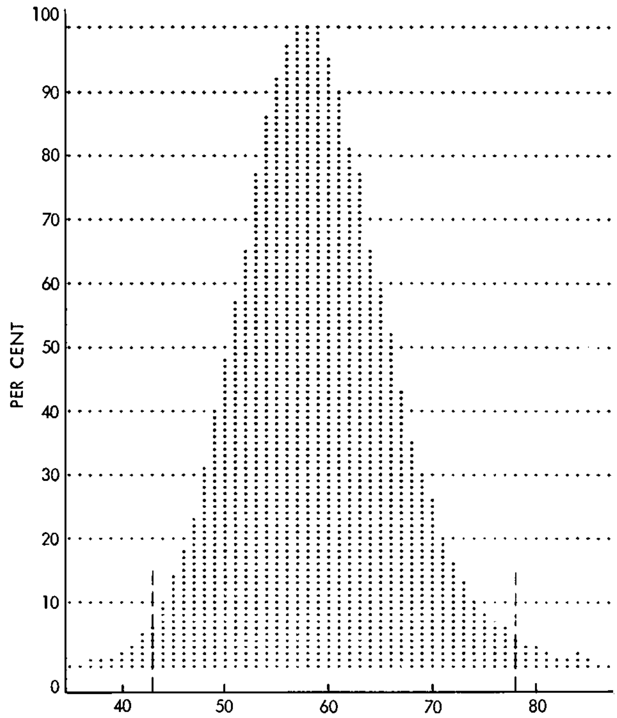

FIGURE 2 Definition of the tails of the histogram. (This histogram belongs to the second image of the focus series, Fig. 7 *b*.) Intensity range (horizontal axis, arbitrary units) corresponds to approximately 0.1 density range. The vertical axis gives the frequency of the data, normalized to maximum frequency = 100%. All pictorial representations show only the data between the marked limits and allow for the saturation of 1% of the data on either side.

For expendiency, we shall use the term "log-abs representation" for expression 34. Because of the logarithmic response of the photo emulsion to light, this representation corresponds to the density distribution in an optical diffraction pattern (diffractogram) of the image $g(\mathbf{r}) = \mathfrak{F}^{-1}\{G(\mathbf{k})\}$. Therefore, expression 34 will also be referred to as the diffractogram of the image $g(\mathbf{r})$.

Processing

The programs involved in the calculation of the complex image are shown in Fig. 3. An area B_n , $1 \leq n \leq N$ containing 256 × 256 elements (324 × 324 A on the object scale) was cut out of the scanned portion of each of the N images of the series. Since the mutual angular orientations of the images had been adjusted before scanning by matching details visible on each image, only the mutual translational positions had to be determined. For this purpose, the cross-correlation matrices,

$$C_{n_1 n_2}(j, l) = \sum_{i,k} I_{n_1}(x_i , y_k)I_{n_1}(x_{i+j} , y_{k+l}), \qquad (35)$$

were directly calculated from 81 × 81 A portions of the B_n using the computer-linked IBM

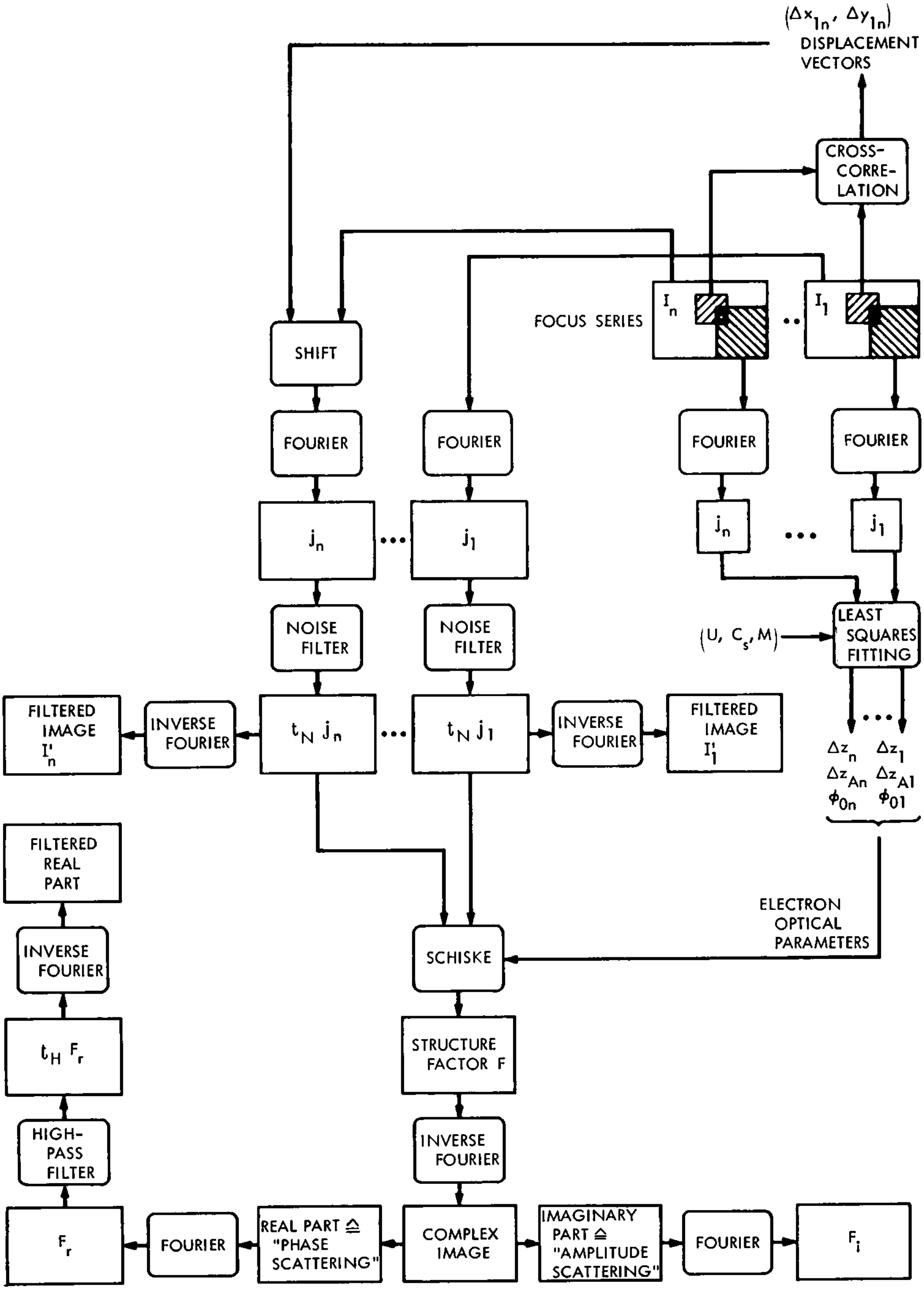

FIGURE 3 Block diagram of the program system. Only two images of the focus series are shown. Different portions of the image are used for the calculation of the cross-correlation matrix and for the least squares fitting: 64 × 64 elements (81 × 81 A) and 128 × 128 elements (162 × 162 A), respectively. The filter functions for high-pass and noise filtering are denoted by t_H and t_N, respectively.

2937 Multiplier-Summation processor.[4] The electron optical parameters were determined for each image using the Fourier transform of a 162 × 162 A portion of the B_n (see preceding section).

Instead of the Fourier integrals, equations 1 and 2, the Fourier sums were calculated, which have equivalent properties with regard to orthogonality and approximation of the represented functions (Hildebrand, 1956 *b*). For these calculations, the algorithm of Cooley and Tukey (1965) was used.

The Fourier transforms $j_n(\mathbf{k})$ of the areas B_n were modified by a spatial filter function $t(\mathbf{k})$,

$$j'_n(\mathbf{k}) = t(\mathbf{k}) j_n(\mathbf{k}), \tag{36}$$

which is described below, and were displayed in the log-abs representation. They can be compared with the familiar light optical diffraction patterns (diffractograms) of electron micrographs from thin carbon films (Thon, 1965). Subsequent inverse transformation of the Fourier transforms (equation 36) yields the modified images of the series, to be compared with the photographic prints of the area B_n on the film and with both parts of the complex image.

Since the scanning system used in this investigation was not designed for low contrast images, a particular problem occurred. In the sample direction and in the direction perpendicular to it, noise is appearing which is of the same order of magnitude as the signal if the contrast is low. As a log-abs representation of the Fourier transform of a scanned image shows (see Fig. 4), the Fourier contributions of this scanning noise are limited to the axes.[5] Because the Fourier transform of an unperiodic object is not concentrated in discrete points in Fourier space as it is in the case of periodic objects, the coefficients along the axes can be set to zero without causing an appreciable information loss. Therefore, the filter function

$$t(\mathbf{k}) = \begin{cases} 0 & \text{for } k_x = 0 \text{ or } k_y = 0, \\ 1 & \text{for } k_x = k_y = 0, \\ 1 & \text{elsewhere,} \end{cases} \tag{37}$$

was applied in equation 36. Moreover, by constructing an artificial aperture, those Fourier coefficients can be set to zero which carry only the high-frequency portion of the film noise and the noise due to the electron intensity fluctuations but no information about the object:

$$t(\mathbf{k}) = \begin{cases} 0 & \text{for } |\mathbf{k}| > k_1, \\ 1 & \text{elsewhere.} \end{cases} \tag{38}$$

In order to determine the optimum value for the aperture radius k_1, the Fourier resolution test (Frank et al., 1970 *b*; Hoppe et al., 1970 *a*) was used. Accordingly, the extension of that

---

[4] Although this method is slower than the Fourier method (Langer et al., 1970), it is preferable because the correlation matrix is calculated for the finite images rather than for two infinite layer lattices with the finite images as unit cells.

[5] This noise contribution is clearly visible in the image when displayed without filtering. It is realized that a similar effect in the Fourier transform is caused by the density steps on the boundary (De Rcsier and Moore, 1970). Inspection of the prints of the focus series shows, however, that the mean optical density is about the same on opposite boundaries. The author believes, therefore, that the "edge effect" gives only minor contributions to the spikes on the Fourier axes.

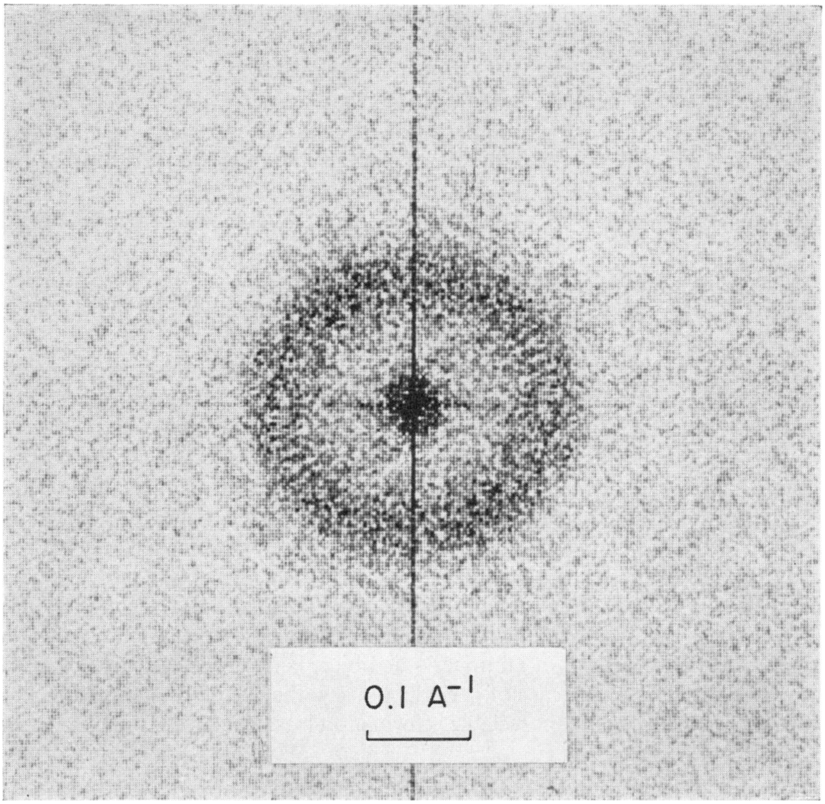

FIGURE 4 Diffractogram of the first image without filtering, showing scanning noise contributions concentrated on the axes.

portion of the spatial spectrum which carries information about the object can be detected by calculating

$$|\mathfrak{F}\{I_{B(1)}(\mathbf{r}) + I_{B(2)}(\mathbf{r} + \Delta\mathbf{r})\}|^2, \qquad (39)$$

where $I_{B(1)}$ and $I_{B(2)}$ are bright-field images of the same object. A has been shown (Frank et al., 1970 *b*; Frank, 1969), a modulation term cos $(2\pi\mathbf{k}\Delta\mathbf{r})$ occurs in expression 39 which makes the Fourier resolution detectable.[6]

The calculation of expression 39 was performed for two electron micrographs of the focus series under investigation (see Figs. 7 *c* and *d*). In the log-abs representation in Fig. 5, the modulation is visible within $|\mathbf{k}| \leq 0.22$ A^{-1} ($\vartheta < 0.81$), corresponding to 4.5 A resolution. A slightly greater value, $k_1 = 0.25$ A^{-1}, was taken in all calculations as the aperture radius of the filter function, equation 38. Subsequently, the parameters of the phase factors were determined using the least squares program mentioned earlier.[7]

---

[6] If the electron micrographs $I_{B(1)}$ and $I_{B(2)}$ are taken with a different focus, the cosine function is replaced by a more complicated function, which, however, can still be used for the detection of the Fourier resolution.

[7] This program was made available by courtesy of the Abteilung Röntgenstrukturforschung am Max-Planck-Institut für Eiweiss- und Lederforschung, Munich, W. Germany.

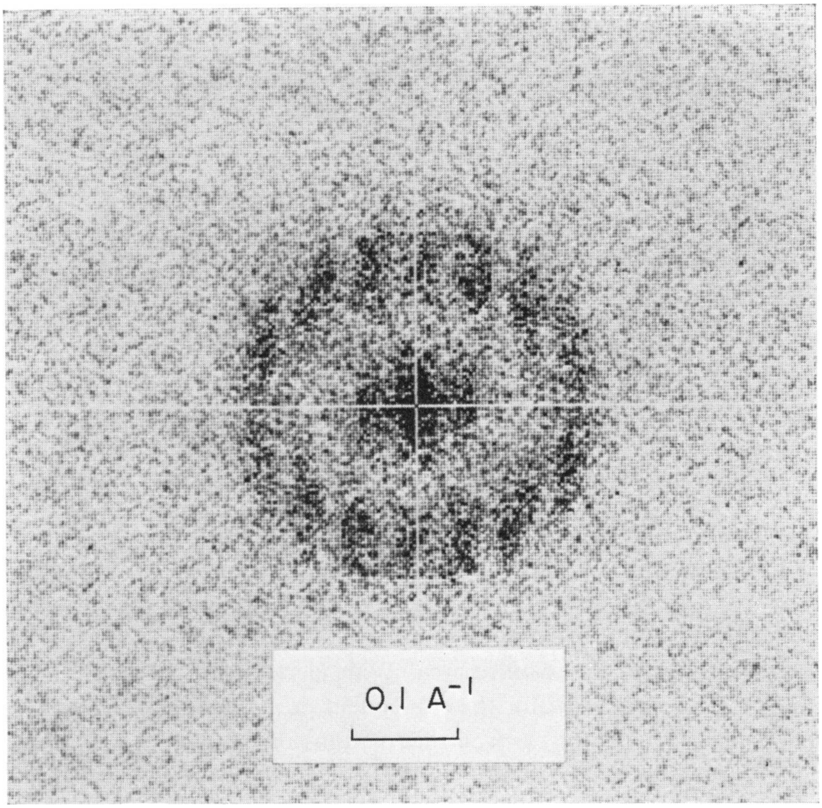

FIGURE 5 Fourier resolution test using two images of the focus series (Figs. 7 *c* and *d*). Displacement, 32 A; modulation extends to 0.22 A^{-1}, corresponding to 4.5 A.

Using the modified Fourier coefficients, equations 36, the structure factor $F(k)$ was calculated by means of equation 23 ("Schiske" program in Fig. 3). The complex image $C(\mathbf{r})$ was obtained by computing the inverse transform. As we expect from the study of equation 23, the imaginary part has no singularity near $\vartheta = 0$ and can be displayed directly. In the real part, on the other hand, the Fourier coefficients predominate near $\vartheta = 0$, and a pictorial representation becomes meaningless. In order to be able to compare the real with the imaginary part at least for the spatial frequency region, $|\mathbf{k}| \geq k_2 = (1.6 \times 10^{-3})/\lambda$, $F_r(\mathbf{k})$ was calculated by inverting equation 18 *a*,

$$F_r(\mathbf{k}) = \mathfrak{F}\{\mathrm{Re}\{C(\mathbf{r})\}\},$$

and was high-pass filtered:

$$F_r(\mathbf{k}) \exp \begin{cases} F_r(\mathbf{k}) \exp\left[-\dfrac{(|\mathbf{k}| - k_2)^2}{\sigma^2}\right] \text{for } |\mathbf{k}| \leq k_2, \\ \text{unchanged elsewhere.} \end{cases} \tag{40}$$

The gaussian function with an appropriate half-width σ was chosen to avoid the cutoff effect.

In order to visualize the radial dependence of $F(\mathbf{k})$ and of its portions $F_i(\mathbf{k})$ and $F_r(\mathbf{k})$, these coefficients were log-abs represented. Part $F_i(\mathbf{k})$ was obtained by reversing equation 18 *b*:

$$F_i(\mathbf{k}) = \mathfrak{F}\{\mathrm{Im}\{C(\mathbf{r})\}\}. \tag{41}$$

From the calculated structure factor, the images of the focus series were, in turn, calculated by applying the phase factors $i \exp[-i\gamma_n]$, inversely transforming, and taking the real part of the result:

$$I'_{B(n)} = \mathrm{Re}\{\mathfrak{F}^{-1}\{iF(\mathbf{k}) \exp[-i\gamma_n]\}\}. \tag{42}$$

These images can be compared with the *original* images of the focus series. For comparison of the diffractograms of the respective images of the original and calculated series, the Fourier transforms of the intensities $I'_{B(n)}$ were calculated and displayed in the usual log-abs representation.

RESULTS

The Input Images

Fig. 6 shows a survey of the scanned area of one electron micrograph. The portion marked by the frame was used for the subsequent processing. Figs. 7 *a–d* show the noise-filtered portions of four electron micrographs of the focus series which have already been brought into the proper mutual position, together with their calculated diffractograms. For comparison, the photographic prints of the same areas are presented in Figs. 8 *a–d*.

As an examination of the diffractograms shows, the axial astigmatism is almost compensated in this series. Since the area in the image occupied by the molecule is very small in comparison with the total area used for calculating the Fourier transform, the phase object contribution from the carbon film dominates the diffractogram.

The least squares program reveals that the defocus value starts at about −80 A and increases by steps of about 120 A. The focus difference of the axial astigmatism Δz_A turns out to be less than 40 A and is therefore neglected in the calculations.

The behavior of $\sin \gamma(\vartheta)$ and $-\cos \gamma(\vartheta)$ for this set of defocus values is illustrated in Figs. 9 *a* and *b*. These functions are the transfer functions for F_r and F_i, respectively (see Reimer, 1969). We realize that the concentration visible near the origins of the diffractograms cannot be explained by the phase properties of the object because the corresponding transfer functions $\sin \gamma_n$ are very small in this region. These low-frequency coefficients have to be attributed partly to the amplitude scattering, which, according to Fig. 9 *b*, is transferred almost without loss, and partly to the inelastic scattering, which is concentrated at low angles.

It is not surprising that the image does not change much within the small Δz range; however, a characteristic Δz dependence of the phase contrast (Thom, 1965)

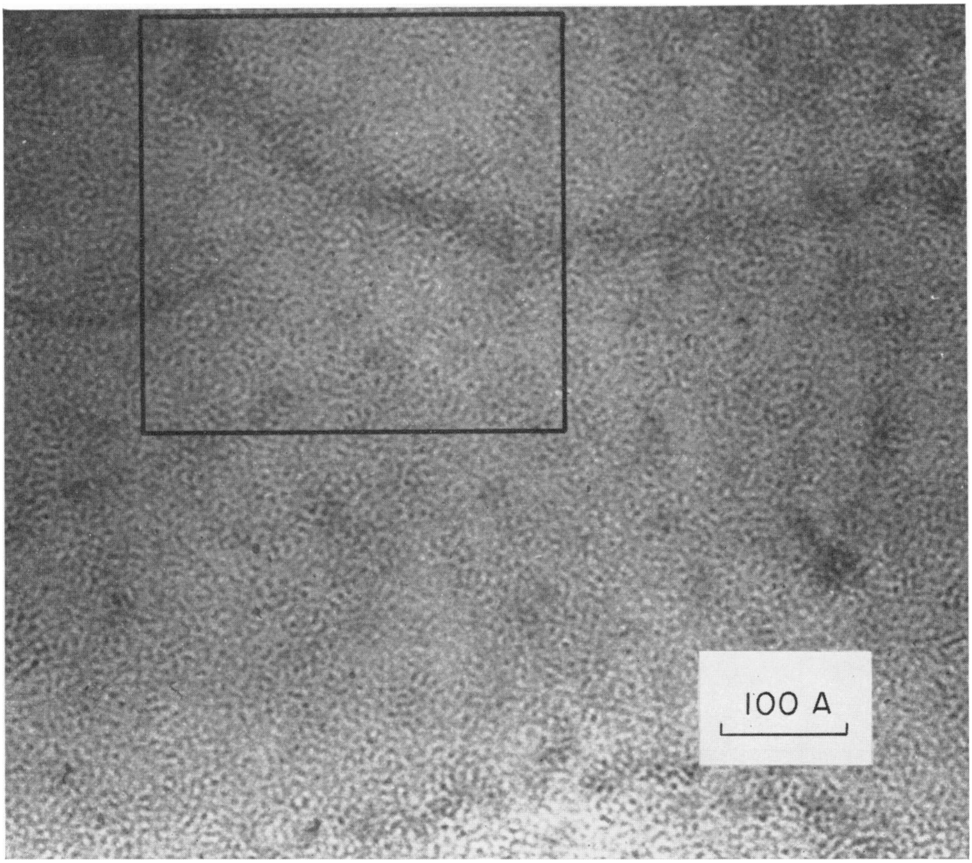

FIGURE 6 Survey of the scanned area. Frame shows the area (324 × 324 A) used for subsequent processing.

can be recognized in the carbon region if the first and the last image of the series are compared (Figs. 8 *a*, *d*). Near the gaussian focus, only details of medium size are apparent. At 280 A, finer details are enhanced and, simultaneously, clusters of very large size become visible as a result of the appearance of a second extremum in the phase-contrast transfer function sin γ (see Fig. 9 *a*).

It is important for the imaging of the stained DNA that the Fourier coefficients responsible for the *over-all* contrast of the heavy atom groups along the molecule do not change significantly within the small focus range (see Fig. 9 *b*). On the other hand, the coefficients transferring the *high resolution* information are considerably affected by the change in the "amplitude contrast" transfer function $-\cos\gamma$ with Δz. Thus, the great changes in the fine details in the region of the molecules are explained. The width of the molecule varies between 36 A (at $\Delta z = -80$ A) and 27 A (at $\Delta z = +280$ A).

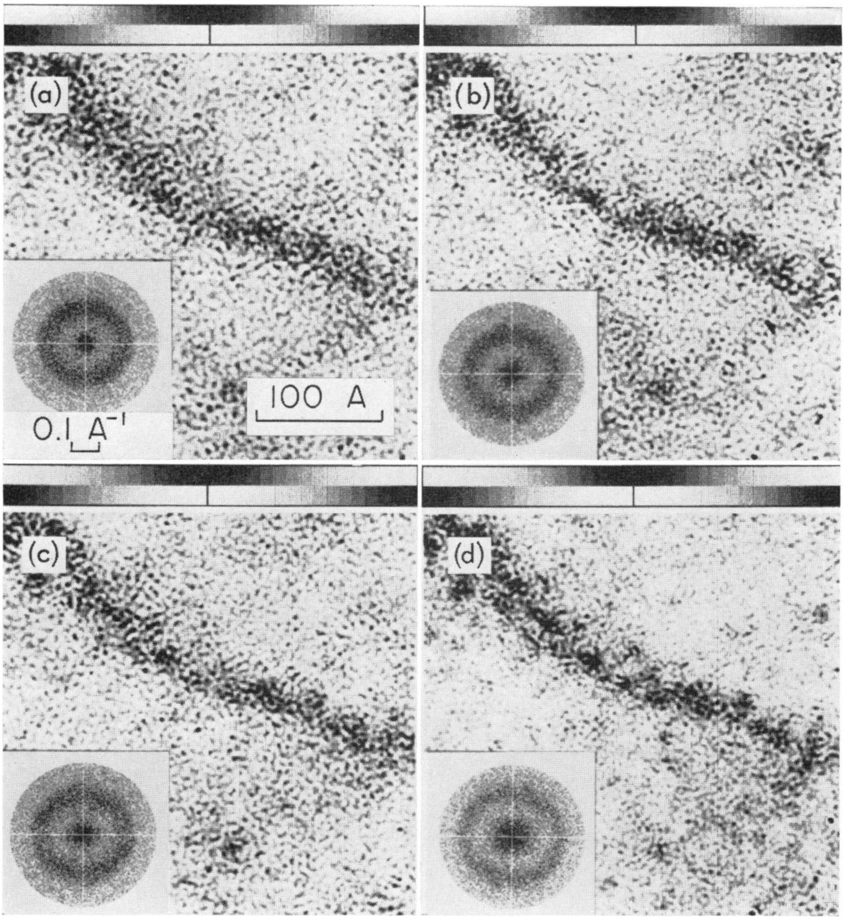

FIGURE 7 Focus series after noise filtering and positioning. High photographic density corresponds to low density on the original electron micrographs. The diffractograms are calculated for the whole area (324 × 324 A). The density calibration represents densities between $d = 0$ and $d = 2$ in steps of 0.125 (see also Figs. 10–13).

The Complex Image

The imaginary and real parts of the complex image are shown in Figs. 10 *a* and *b* together with their calculated diffractograms, and the diffractogram of the complex image is presented in Fig. 10 *c*. The real part was high-pass filtered, as described earlier, and is illustrated in Fig. 10 *d*, together with the diffractogram, which shows the effect of the filter function. First studying the Fourier transforms, we notice that their radial dependence emerges in the way we would expect from the shape of f' and f'' (see Fig. 1): $|F_r|$ decreases with increasing ϑ, whereas $|F_i|$ increases at the same time. According to our discussion in the first section, however, the high values of $|F_r|$ for $\vartheta \leq 0.2 \times 10^{-2}$ must be attributed to the analytical behavior of formula 23 near the origin since $\sin \gamma_m \approx 0$ in this region (see Fig. 9 *a*).

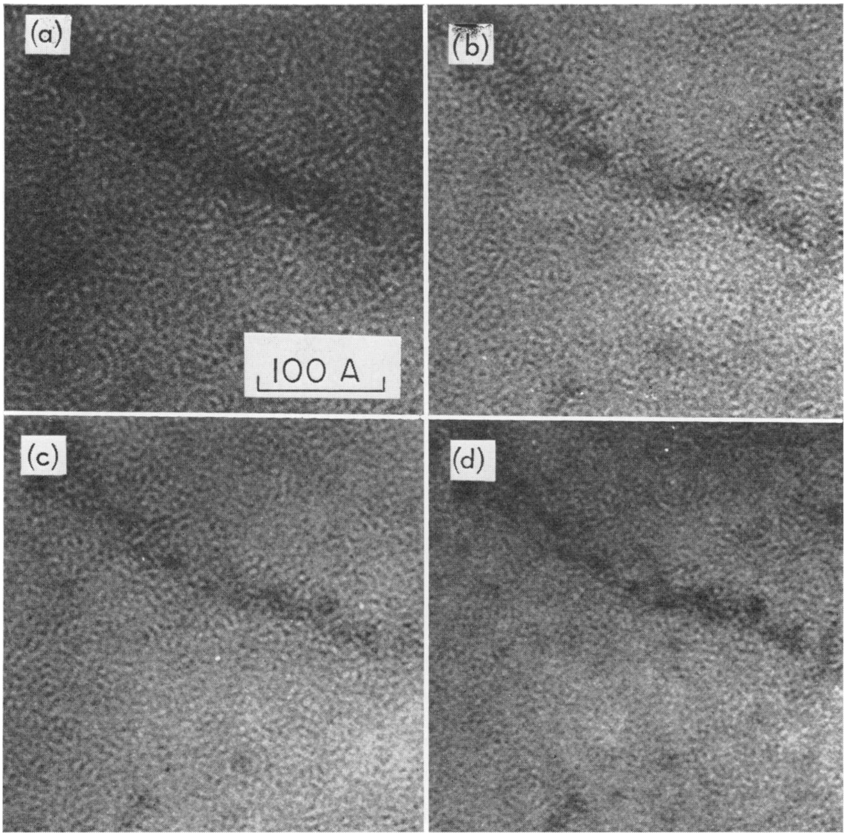

FIGURE 8 Photographic prints of the focus series.

The real image (Fig. 10 *b*) shows the predominance of low-frequency coefficients. We can, in fact, regard it as an overemphasized representation of the variations in the thickness of the carbon foil. The cloudy intensity distribution does indeed approximately agree with the over-all intensity variations visible on the images of the focus series, especially in Fig. 7 *a*. After application of the high-pass filter described earlier, the real image appears very granular, and the contributions of the molecule are still not discernible. We can conclude that the real images of the uranium atoms or of groups of uranium atoms, respectively, are obscured by the image of the carbon film, at least if only the scattering angles $\vartheta \geq 0.16 \times 10^{-3}$ rads are passed.

Since it was the imaginary part of the image that was of special interest, no further effort was made to analyze the properties of the real image.

The Fourier transform of the imaginary image (see Fig. 10) has a gap in the spatial frequency range corresponding to $0.27 \leq \vartheta \leq 0.46 \times 10^{-2}$ rads and is concentrated in the high-frequency range corresponding to $0.46 \leq \vartheta \leq 0.7 \times 10^{-2}$ rads. In the gap of the spatial spectrum, a latticelike distribution of coefficients is apparent which can also be detected in the diffractogram of the second image of

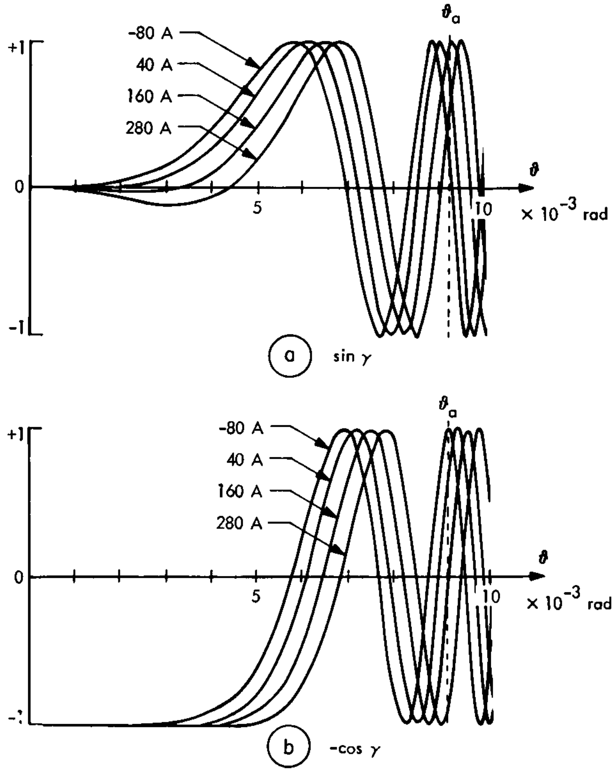

FIGURE 9 (*a*) Transfer functions for "phase objects," sin γ_n. (*b*) Transfer functions for "amplitude objects," $-\cos \gamma_n$. Aperture $\vartheta = 9.2 \times 10^{-3}$ rads used for calculation is marked by a dotted line.

the series (Fig. 7 *b*). It is assumed that this pattern contains structural information about the image of the molecule.

Since formula 23 has no singularity in the aperture region, we are, at first, inclined to assume that the preponderance of the high-frequency coefficients is due to the structure of the amplitude part of the object. This would indicate that distances between 5.3 and 8 A occur most frequently. An examination of the Fourier transform of an isolated *carbon* portion of the image, however, showed the same high-frequency zone. The possibility that this zone arises from structural properties of the object can therefore be excluded. Another explanation is given (*a*) by the ϑ dependence of f'', which, in the case of free atoms, for instance, accounts for the increase in $|F_i|$ by a factor of about 1.5 within the aperture (see Fig. 1); and (*b*) by the high resolution contribution to the imaginary scattering due to the curvature of the Ewald sphere.

The imaginary image (Fig. 10 *a*) was represented in different modes in order to visualize the highest intensity maxima. In Figs. 11 *a* and *b*, only 60 and 40% of the highest intensity values are represented.

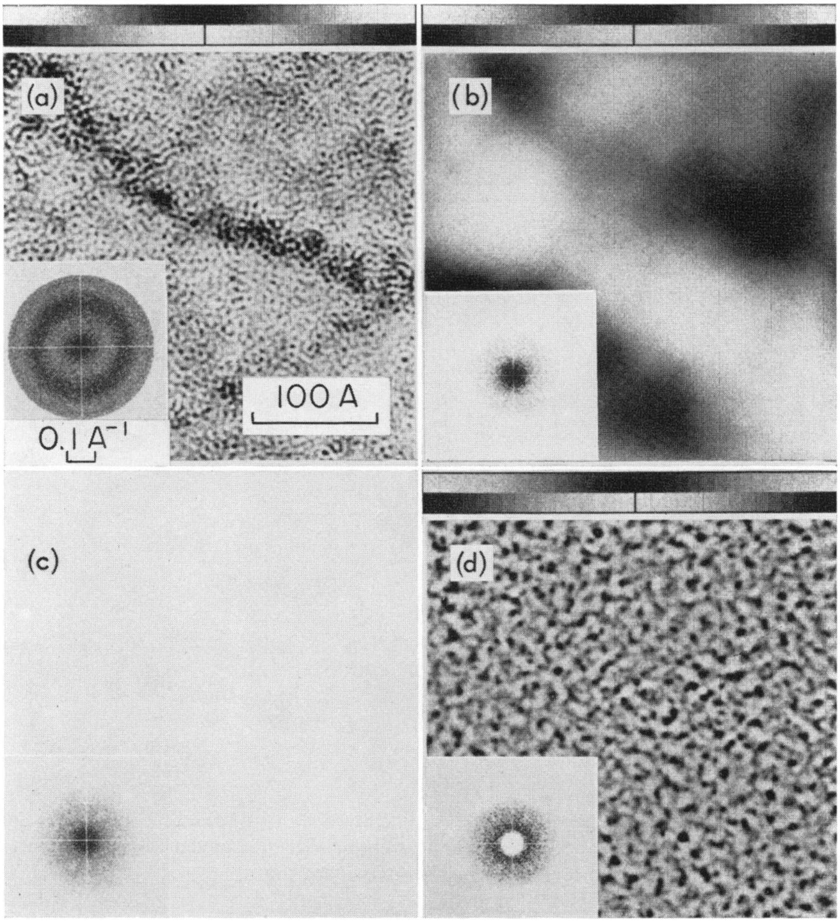

FIGURE 10 (*a*) Imaginary image, representing the contributions due to the imaginary portion of scattering. High photographic density represents high intensity. (*b*) Real image, representing the contributions due to the real portion of scattering, without filtering. (*c*) Diffractogram of the complex image. (*d*) Real image, after high-pass filtering. The diagonal pattern in *b* is an artifact produced by interference between VFC output raster and the screen used for photographic reproduction.

With the aid of these additional representations, some features can be discerned in the DNA image which are thought to be related to the structure of the molecule, although these features are somewhat obscured by an irregular pattern of intensity maxima.

For comparison, the result of an idealized model calculation done by Welton (Welton, 1970) was reproduced in Fig. 11 *c* on the same scale.[8] Welton calculated the image of one repeat distance (33.6 A) of DNA (polyadenylic-polythymidylic acid [poly A-T]) on a carbon foil, with uranium atoms attached to each phosphate

---

[8] Courtesy of Dr. T. A. Welton.

and each thymine group (U = 150 kev, C_s = 1 mm, defocus at optimum contrast). The straight portion of the molecule on the right-hand side of Figs. 10 *a* and 11 *a* and *b* respectively, has some similarity to the model image, although its intensity maxima are irregularly distributed. This result might well be attributed to the non-uniform distribution of the uranium atoms.

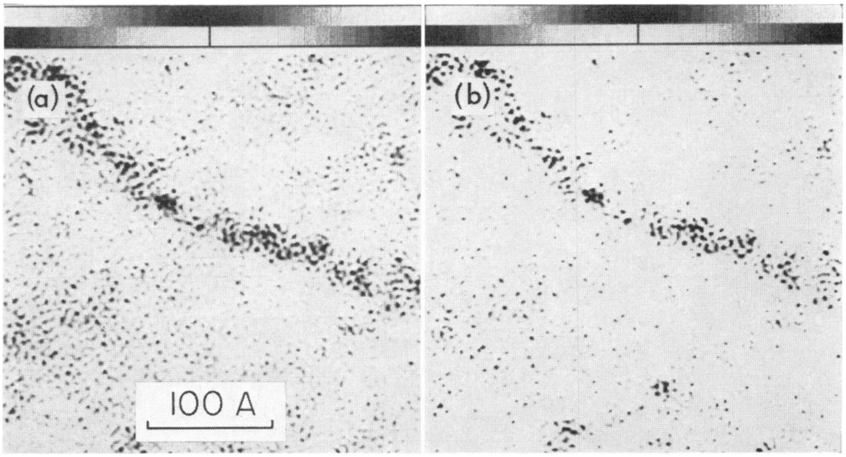

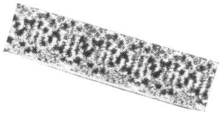

FIGURE 11 *c*

FIGURE 11 Imaginary image of Fig. 10 *a*. (*a*) Only 60% of the highest intensity values represented; (*b*) only 40% represented. (*c*) Results of Welton's model calculation on the same scale as Figs. 11 *a* and *b*. Three repeat distances are shown.

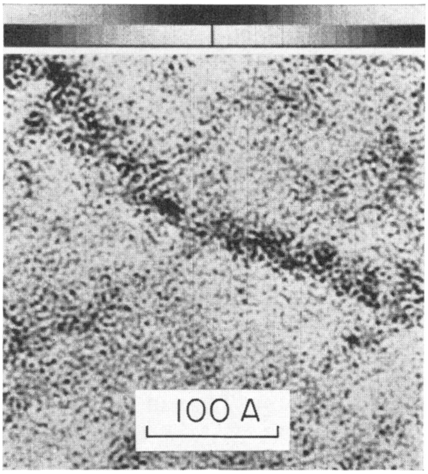

FIGURE 12 Imaginary image, calculation with all Δz values shifted by $+120$ A, for comparison with Fig. 10 *a*.

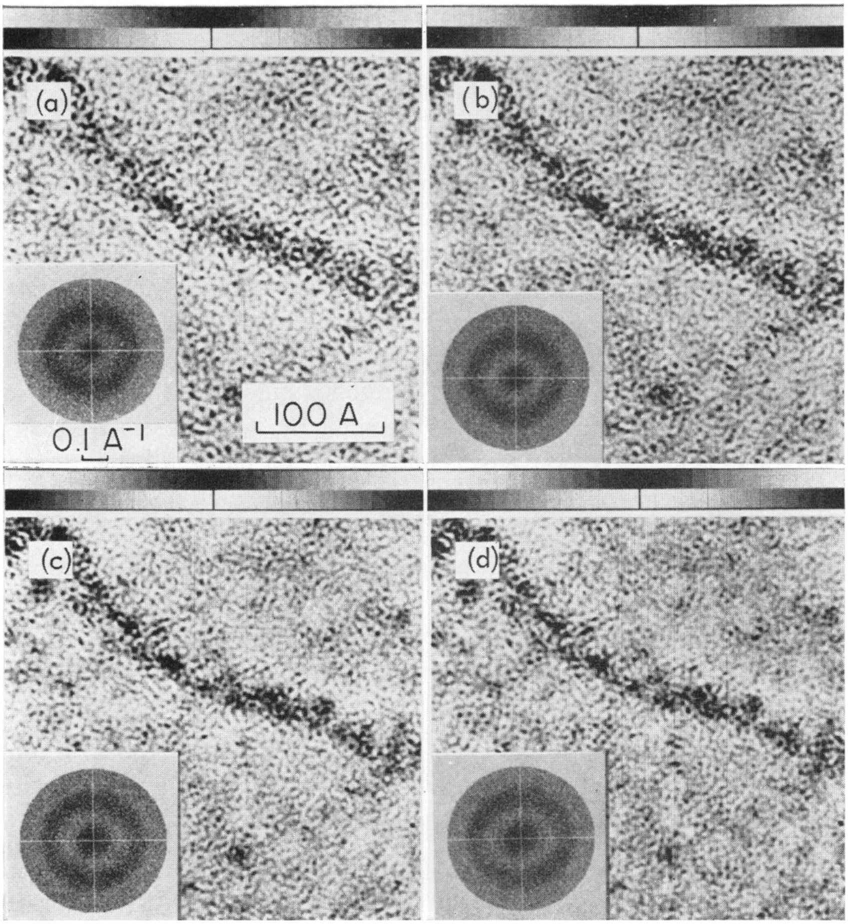

FIGURE 13 Focus series, calculated from the structure factor, for comparison with the original series, Figs. 7 *a–d*.

The structural features observed in the image are not critically dependent on the absolute focus value within a certain range. In order to show this, the same calculation (equation 23) was repeated with a different set of defocus values (+40, +160, +280, +400 A); the resulting imaginary image is presented in Fig. 12.

The imaginary image in Fig. 10 *a* shows also that the contrast of the molecule on the carbon background is enhanced when compared with its contrast in the input images of the series shown in Figs. 7 *a–d*. The ratios

$$\frac{\Delta I_{\mathrm{DNA}}}{\Delta I_{\mathrm{Carbon}}} = \frac{\text{Intensity variation due to the stained DNA molecule}}{\text{Intensity variation in the carbon background}}$$

were calculated from small areas (25 × 25 A) of the imaginary image and the input images, and the values 1.4 and 1.05 were found, respectively. We see that the expected separating effect (see first section) is less than it would be for single uranium atoms on a carbon film consisting of 30 atomic layers. Besides the curvature of

Ewald's sphere, three main reasons for this fact may be considered. First, the atomic scattering amplitude changes if the atoms are bound in the solid state, as mentioned earlier. Second, the inelastic scattering has been neglected in the theory. Therefore, the low resolution Fourier coefficients may be misinterpreted by using Schiske's formula. Third, the preparation of the specimen may result in an unknown number of uranyl groups being attached to the carbon foil, and the intensity fluctuations caused by their images may have been misinterpreted as being due to the carbon background. This ambiguity can be overcome by a carefully controlled preparation technique.

The focus series was calculated from the calculated structure factor, assuming $\Delta z_A = 0$ and $\Delta z = -80 \cdots +280$ A. The result is shown in Figs. 13 *a–d*, together with the corresponding diffractograms. The similarity to the original series and its diffractograms (Fig. 7), respectively, is fairly good. This may be checked by comparing high resolution details in the respective images. Some artifacts produced by the copying and scanning, such as the triangle-shaped detail on the right-hand side of Fig. 7 *b*, are now appearing in each image, thus showing the averaging which takes place in equation 23.

It is realized that this visual assessment is insufficient and that it should be replaced by application of quantitative criteria similar to those which are used in X-ray crystallography.

Special thanks are due to Dr. Robert Nathan for enabling me to carry out this task, as well as for his cooperation and assistance.

Grateful acknowledgment is made to Dr. Walther Stoeckenius for generously providing me with the DNA series and for his willing cooperation.

I would like to thank Dr. Robert Glaeser for a detailed discussion.

This work was undertaken in the Image Processing Applications Group, Science Data Analysis Section, of the Jet Propulsion Laboratory, California Institute of Technology.

This work was executed as part of the Harkness Fellowship Program of The Commonwealth Fund and partly supported by the National Institutes of Health.

Received for publication 10 June 1971.

REFERENCES

Beer, M., and E. N. Moudrianakis. 1962. *Proc. Nat. Acad. Sci. U.S.A.* **48**:409.
Billingsley, F. C. 1970. *J. Appl. Opt.* **9**:289.
Billingsley, F. C. 1971. *Advan. Opt. Electron Microsc.* **4**:127.
Billingsley, F. C., and J. J. Volkoff. 1969. *NASA Tech. Brief.* 69-10568.
Cooley, J. W., and J. W. Tukey. 1965. *Math. Comput.* **19**:296.
Cosslett, V. E. 1965. *Lab. Invest.* **14**:271.
Crewe, A. V., and J. Wall. 1970. *J. Mol. Biol.* **48**:375.
Crick, R. A., and D. L. Misell. *Brit. J. Appl. Phys.* **4**:1.
De Rosier, D. J., and P. B. Moore. 1970. *J. Mol. Biol.* **52**:355.
Erickson, H. P., and A. Klug. 1970. *Ber. Bunsenges. Phys. Chem.* **74**:1129.
Eisenhandler, C. B., and B. M. Siegel. 1966. *J. Appl. Phys.* **37**:1613.
Fiskin, A. M., and M. Beer. 1968. *Science (Washington).* **159**:1111.
Frank, J. 1969. *Optik (Stuttgart).* **30**:171.

Frank, J., P. H. Bussler, R. Langer, and W. Hoppe. 1970 *a*. 7th International Congress on Electron Microscopy. Grenoble, France. **1**:17.

Frank, J., P. H. Bussler, R. Langer, and W. Hoppe. 1970 *b*. *Ber. Bunsenges. Phys. Chem.* **74**:1105.

Glaeser, R. M., T. F. Budinger, P. M. Aebersold, and G. Thomas. 1970. 7th International Congress on Electron Microscopy. Grenoble, France. **1**:463.

Glauber, R., and V. Schomaker. 1953. *Phys. Rev.* **89**:667.

Haase, J. 1968. *Z. Naturforsch. A.* **23**:1000.

Haase, J. 1970 . *Z. Naturforsch. A.* **25**:1219.

Hanssen, K. J. 1965. *Z. Angew. Phys.* **19**:215.

Hartmann, R. E., and R. S. Hartmann. 1971. Proceedings of the 29th Annual Meeting of the Electron Microscope Society of America, Boston, Mass. 74.

Hildebrand, F. B. 1956 *a*. Introduction to Numerical Analysis. McGraw-Hill Book Company, New York. 258.

Hildebrand, F. B. 1956 *b*. Introduction to Numerical Analysis. McGraw-Hill Book Company, New York. 373.

Hoppe, W. 1970. *Acta Crystallogr. Sect. A.* **26**:414.

Hoppe, W., R. Langer, A. Hirt, and J. Frank, 1970 *a*. 7th International Congress on Electron Microscopy, Grenoble, France. **2**:5.

Hoppe, W., R. Langer, and F. Thon. 1970 *b*. *Optik (Stuttgart)*. **30**:538.

Ibers, J. A., and J. A. Hoerni. 1962. International Tables of X-Ray Crystallography. Kynoch Press, Birmingham, England. **3**:218.

Ibers, J. A., and B. V. Vainshtein. 1962. International Tables of X-Ray Crystallography, Kynoch Press, Birmingham, England. **3**:222.

Koller, T. 1971. *Biophys. Soc. Annu. Meet. Abstr.* **11**:216a.

Langer, R., J. Frank, A. Feltynowski, and W. Hoppe. 1970. *Ber. Bunsenges. Phys. Chem.* **74**:1120.

Lenz, F. 1954. *Z. Naturforsch. A.* **9**:185.

Messiah, A. 1962. Quantum Mechanics. North Holland Publishing Co., Amsterdam. **2**:866.

Moudrianakis, E. N., and M. Beer. 1965. *Proc. Nat. Acad. Sci. U.S.A.* **53**:564.

National Aeronautics and Space Administration documentation. 1968. Ref. 324-IPG/1067.

Ottensmeyer, F. P. 1969. *Biophys. J.* **9**:1144.

Reimer, L. 1969. *Z. Naturforsch. A.* **24**:377.

Reimer, L., and K. H. Sommer. 1968 *a*. 4th European Regional Conference on Electron Microscopy. Rome, Italy. **1**:63.

Reimer, L., and K. H. Sommer. 1968 *b*. *Z. Naturforsch. A.* **23**:1569.

Scherzer, O. 1949. *J. Appl. Phys.* **20**:20.

Schiske, P. 1968. 4th European Regional Conference on Electron Microscopy. Rome, Italy. **1**:145.

Thon, F. 1965. *Z. Naturforsch. A.* **20**:154.

Uyeda, R. 1955. *J. Phys. Soc. Jap.* **10**:256.

Welton, T. A. 1970. Proceedings of the 28th Annual Meeting of the Electron Microscope Society of America, Houston, Tex. 32.

Whiting, R. F., and F. P. Ottensmeyer. 1971. *Biophys. Soc. Annu. Meet. Abstr.* **11**:215a.

Williams, R. C., and H. W. Fisher. 1970. *J. Mol. Biol.* **52**:121.

Zeitler, E., and H. Olsen. 1967. *Phys. Rev.* **162**:1439.

Zobel, C. R., and M. Beer. 1961. *J. Biophys. Biochem. Cytol.* **10**:335.